Electronic structure of NiAl

S.-C. Lui
Laboratory for Research on the Structure of Matter, University of Pennsylvania, Philadelphia, Pennsylvania 19104

J. W. Davenport
Department of Physics, Brookhaven National Laboratory, Upton, New York 11973

E. W. Plummer
Laboratory for Research on the Structure of Matter, University of Pennsylvania, Philadelphia, Pennsylvania 19104

D. M. Zehner
Solid State Division, Oak Ridge National Laboratory, Oak Ridge, Tennessee 37831

G. W. Fernando
Department of Physics, Brookhaven National Laboratory, Upton, New York 11973
(Received 14 December 1989; revised manuscript received 3 April 1990)

The valence-band structure of nickel aluminum was measured by use of angle-resolved photoemission with synchrotron radiation and calculated using the local-density approximation. The overall agreement between theory and experiment is remarkably good—much better than for pure nickel. This means that the "self-energy" corrections are significantly less in NiAl than in pure nickel. The core-level binding energies in NiAl are compared experimentally and theoretically with the equivalent levels in Ni and Al. Surprisingly, the Ni core shifts to higher binding energy and the Al to lower as if charge were transferred from Ni to Al—opposite to the direction predicted from electronegativity. These observations are discussed in terms of bonding in NiAl.

I. INTRODUCTION

The purpose of this paper is to present an experimental and theoretical study of the electronic structure of nickel-aluminum. NiAl is one of the simplest metallic compounds—it crystallizes in the CsCl structure, which consists of two interpenetrating simple-cubic lattices. It has a relatively large heat of formation, 0.61 eV/atom,[1] so that single crystals of different orientations are relatively easy to prepare. Since it is formed from two elemental metals whose electronic properties measured by photoemission have been very well studied,[2,3] the effects of compound formation on the electronic states can be readily isolated. Aluminum is one of the classic examples of a nearly-free-electron metal and its electronic structure can be understood in terms of plane waves and a simple pseudopotential.[4] Nickel is a classic example of a transition metal whose electronic structure consists of a relatively narrow $3d$ band crossing and hybridizing with a nearly-free-electron sp band.[5] The d-band width is ≈ 4 eV, which places it on the borderline between "extended" and "localized" behavior (though these terms are not precisely defined). For example, the photoelectron spectra of pure nickel show a pronounced narrowing (relative to band-structure calculations[2,6,7]) and a "two-hole satellite" feature,[2,8,9] which are indicative of strong, on-site Coulomb interactions.[10] The nickel is, of course, ferromagnetic and has a Curie temperature of 627 K,[11] while NiAl is nonmagnetic[12] (Ni_3Al is, however, ferromagnetic[13,14]). While the lattice constant, magnetic moment ($0.56\mu_B$/atom), and the Fermi surface of nickel can all be understood in terms of a band picture, the Curie temperature (which is much smaller than the exchange splitting) and the nature of the electronic structure above the Curie temperature are still not understood.

Since the nickel atoms in NiAl are farther apart than in pure Ni, the d states should be more localized and the d band should be narrower. However, NiAl is a good metal which should be describable by a band theory. In fact, we will show that the difference between the calculated and measured bands is significantly less than in pure Ni, indicating that correlation effects not included in the local-density approximation are less important (even though the bands are narrower). We attribute this difference to the filling of the d band and to the fact that filled bands are better described in a band theory than partially filled ones.[15] Both the x-ray- and uv-photoemission results[16–20] as well as early band-structure calculations[21–24] show that the Ni d band in NiAl is filled and that the density of states at the Fermi level is low. Since the Pauli electronegativity of nickel is 1.9 while that of aluminum is 1.5, a filled Ni d band would naively be taken to imply that electrons are transferred from the Al to the Ni. Actually, both experiment and theory in this paper point to electron transfer from nickel to aluminum. The filling of the d band is supported in our calculations by an increase in the d population upon going from Ni to NiAl. However, there is a larger transfer among the sp electrons from the *opposite* direction (i.e.,

from Ni to Al), leading to a net transfer from nickel to aluminum. This is consistent with the observed core-level shifts, which are in the direction of larger binding energy for the nickel and smaller binding energy for the aluminum. Shifts to the lower binding energy are usually attributed to an increase in electron number at a site which increases the Coulomb repulsion with the cores and reduces the binding energy.

The calculated band structure is shown in Fig. 1. The symmetry at major points is indicated. The energy scale is relative to E_F in units of eV. For bulk NiAl, there are 13 valence electrons per unit cell which fill six initial-state bands, with the seventh band being partially occupied. The Fermi surface extends to the second Brillouin zone, except in the ΓR direction, where hole pockets develop around the zone corners. Free-electron-like character of the initial-state bands is observed both at the bottom of the band and above the Fermi level. These bands are made up of mostly Al s and p states. The Ni d bands are primarily in the energy range between -1 and -4 eV and there is some p-d mixing in this range. The d bands of NiAl lie approximately 1.5 eV below the Fermi level, illustrating the d-band filling of the alloy. In contrast, the energy-band structure of Ni, such as that given by Wang and Callaway,[26] has the Fermi level lying in the region of high d density of states.

It is obvious that the valence-band structure and the total density of states of NiAl are considerably different from that of Ni. In this paper we shall discuss a detailed measurement of the valence-band structure of NiAl. By comparing between the measured and calculated band structures, we can assess the importance of many-body effects in this alloy system. Finally, we shall discuss the bonding of the NiAl alloy system by comparing the measured and calculated core-level shifts and illustrate the significance of p-d hybridization by focusing on a specific region in the valence-band structure.

This paper is organized as follows. In Sec. II we discuss the calculational procedure. In Sec. III we give a description of the experimental apparatus and sample preparation. A brief discussion on the use of angle-resolved photoemission to measure bulk band dispersion is given in Appendix A.

In Sec. IV we present the bulk band structure and Fermi-surface measurements. The bulk and surface Brillouin zones of low-index surfaces are given in Appendix B. A detailed description of the data-analysis procedure is presented in Ref. 27. In Sec. V we discuss the many-body effects and the bonding mechanism of this alloy system. Conclusions are given in Sec. VI and a discussion of spin-orbit splitting is given in Appendix C.

II. CALCULATIONAL PROCEDURE

The calculations reported in this paper have been performed using the linear-augmented Slater-type-orbital method (LASTO).[28] This is a technique for solving the Schrödinger equation in which a Bloch sum of Slater-type

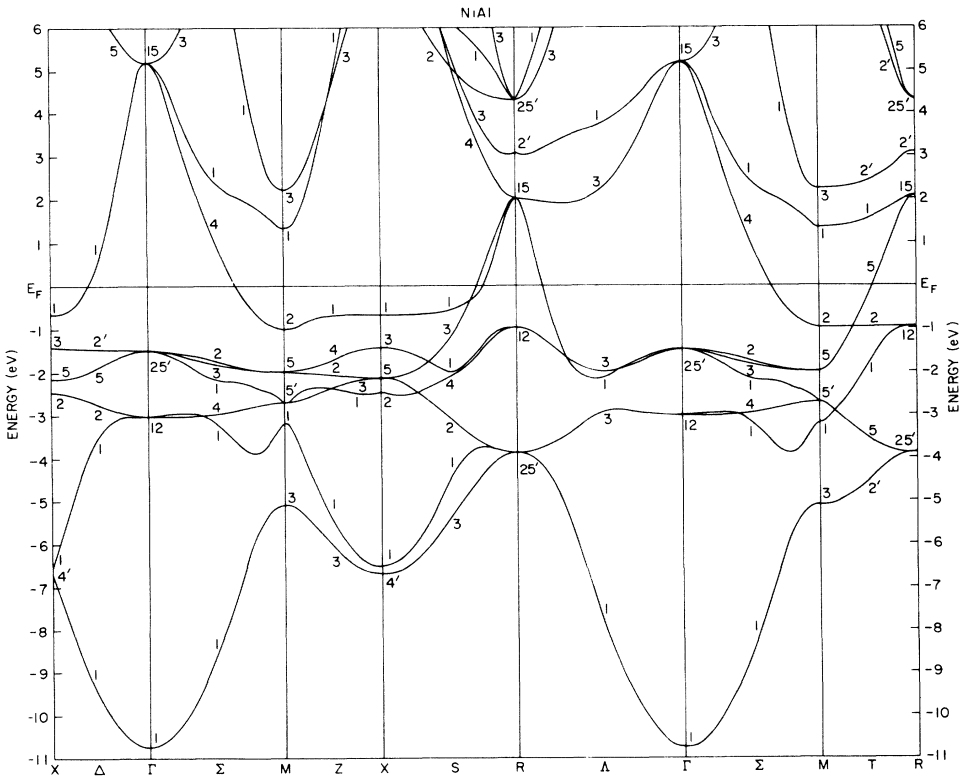

FIG. 1. Calculated bulk band structure of NiAl.

orbitals is used to span the space between atoms and a numerical basis set is used to span the space near the atomic nuclei. The Slater-type orbitals have the form

$$\phi(\mathbf{r}) = r^{n-1}\exp(-\zeta r)Y_{lm} , \quad (1)$$

where Y_{lm} is a spherical harmonic and the ζ's are chosen to minimize the total energy of the metallic elements. The technique has been previously applied to the 5*d* metallic elements, many 5*d*-5*d* alloys,[29] and Cu_3Au.[30] The main difference from previous work is that the full potential was used so that there were no shape approximations made to the density and potential. The technique is described in detail elsewhere,[31] but basically follows the approach used in the full-potential linear-augmented-plane-wave method as described, for example, by Weinert.[32] For the present calculation, a basis set called "double ζ plus polarization functions" was used. This included 3*s*, 3*p*, 4*s*, 4*p*, and 3*d* functions on the aluminum, and 3*d*, 4*s*, 4*p*, 4*d*, 5*s*, 5*p*, and 4*f* functions on the nickel. This leads to a 38×38 secular matrix. The ζ's are listed in Table I. The lattice constants were taken to be the experimental ones, i.e., $a_{Ni}=3.52$ Å, $a_{Al}=4.05$ Å, and $a_{NiAl}=2.88$ Å.

The Brillouin zone was sampled at 35 special **k** points, and the density and potential constructed by broadening and partially occupying the levels near the Fermi level. For calculations of pure Ni and Al (in the fcc structure), the same basis sets were used, but 110 **k** points were sampled in the irreducible wedge of the Brillouin zone.

To construct a density of states, each eigenvalue was broadened with a Gaussian with a full width at half maximum of 0.25 eV. The heat of formation is obtained by taking the difference in total energy of the NiAl and the sum of the energies of Ni and Al. The result is −0.79 eV/atom. This should be corrected by +0.04 eV/atom to account for the fact that our calculation on fcc nickel was nonmagnetic. Therefore the actual heat of formation is −0.75 eV/atom. This is in good agreement with the calculations of Williams *et al.*[33] (−0.74 eV/atom), but is larger than the experimental value −0.61 eV/atom. The discrepancy with experiment is typical of the local-density theory, which tends to overestimate bond energies.

The density of states of NiAl is shown in Fig. 2, where it is compared with that of fcc nickel and also simple-cubic (sc) nickel with the lattice constant equal to that of NiAl. The large peak in each case is identified with the predominantly Ni *d* band. According to the moment rules,[34] one expects the bandwidth to vary as $\sqrt{z}\,t$, where z is the number of like neighbors and t the average hopping integral. t is expected to vary like R^{-5}, where R is the Ni-Ni distance. Using the lattice constants quoted earlier, the ratio of the bandwidths should therefore be

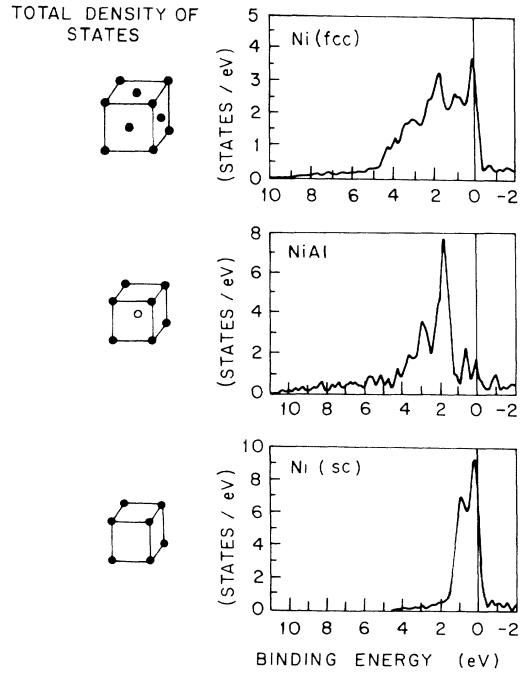

FIG. 2. Calculated total density of states of face-centered-cubic Ni, NiAl (CsCl structure), and simple-cubic Ni.

$$\frac{W_{NiAl}}{W_{Ni}} \sim \left[\frac{6}{12}\right]^{1/2}\left[\frac{2.49\ \text{Å}}{2.88\ \text{Å}}\right]^{5} \approx 0.34 . \quad (2)$$

A crude estimate from the density-of-states plot (Fig. 2) is $W_{Ni}\sim 5.6$ eV, while for sc nickel W_{Ni} is ~ 2.0 eV, leading to a reduction which is close to the predicted value. For NiAl the bandwidth is ~ 2.9, significantly larger than for sc nickel, indicating the importance of Al *p* – Ni *d* hybridization.

III. EXPERIMENTAL PROCEDURE

The angle-resolved photoemission experiments were carried out at the National Synchrotron Light Source (NSLS) at Brookhaven National Laboratory using radiation from the 750-MeV VUV storage ring. The radiation was dispersed by a dual toroidal-grating monochromator yielding photons in the $10<\hbar\omega<120$ eV range.[35] Electrons were energy-analyzed with a hemispherical electrostatic analyzer having an acceptance angle of ±2°. Details of the angle-resolved analyzer and experimental chamber were described elsewhere.[36] The bulk band structure of NiAl was measured in the photon-energy range 12–120 eV. The combined instrumental resolution (photon and electron) is ≈130 MeV for $\hbar\omega<35$ eV and

TABLE I. Zeta values.

Ni	3*d*	2.3	4*s*	1.0	4*p*	1.0	4*f*	1.6
	4*d*	2.6	5*s*	2.0	5*p*	2.0		
Al	3*s*	0.8	3*p*	0.8	3*d*	1.2		
	4*s*	1.0	4*p*	1.0				

increases linearly with photon energy to ≈ 300 meV at $\hbar\omega = 60$ eV.

The data presented in this paper were taken from the three low-index surfaces—(100), (110), and (111) faces—of NiAl. All three crystals were cut from the same NiAl ingot, which has a composition of 50.6 ± 2.0 at. % Al.[37] This composition was determined by Paschen optical-emission spectroscopy and the use of standard solutions. In addition, spark-source mass spectroscopy was invoked to ensure that there were no major impurities in the sample (total < 100 ppm weight concentration). The NiAl crystals were cleaned by neon-ion bombardment (1-keV Ne^+, 7–8 $\mu A/cm^2$). Since Al atoms were preferentially sputtered, annealing was necessary to restore and reproduce a well-ordered surface with a (1×1) low-energy electron diffraction (LEED) pattern. The sputtered samples were annealed to 950°C for (100) and to 850°C for (110) and (111). The Ni($2p$)-to-Al($1s$) Auger-peak-height ratio was measured for each crystal prior to the photoemission experiment. The Ni-to-Al Auger-peak-height ratio was found to be 2.86, which corresponds to an average surface stoichiometry of 50:50. Initial cleaning of each crystal took from 6 to 10 h to sputter off the surface oxide layer. The typical operating pressure of the angle-resolved chamber was $(1-2) \times 10^{-10}$ Torr. During the course of the experiment, the (111) and (100) crystals were repeatedly cleaned at 30–60-min intervals due to oxygen buildup. The (110) crystal, however, stayed clean for up to 3 h. The cleanliness of the surface was monitored by the appearance of the O $2p$ peak at 6–7 eV below the Fermi level.

IV. EXPERIMENTAL RESULTS

A. Dispersion

The bulk Brillouin zone of NiAl is simple cubic, as shown in Fig. 3. The six symmetry directions in the irreducible wedge of the Brillouin zone are three from the zone center (Γ) to the zone boundary and three along the zone face. Dispersion of bulk bands along ΓR, ΓM, and ΓX directions can be obtained by collecting photoemitted electrons normal to the surface using the (111), (110), and (100) faces of NiAl, respectively. Off-normal-emission measurements are done to obtain dispersions of bulk bands along XM, MR, and XR. The binding energies for bands at high-symmetry points, for example, the R point at the zone corner, can be obtained from normal emission along ΓR using NiAl(111) or from off-normal-emission measurement along MR and XR using NiAl(100) and NiAl(110), respectively. Thus, the two different measurements (normal and off-normal) can serve to cross-check the energies obtained for high-symmetry points. A brief discussion on the use of angle-resolved photoemission to measure bulk-band dispersion is given in the Appendix A. Appendix B presents figures showing the relationship between the two-dimensional surface Brillouin zone (SBZ) and the three-dimensional bulk Brillouin zone. These figures are used to determine which part of the bulk band can be measured. Details of the measurements and an in-depth description of the measurement procedure along ΓR, ΓM, and ΓX and MX can be found in Ref. 27.

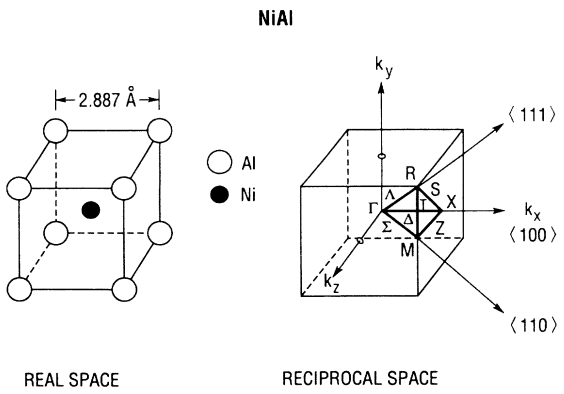

FIG. 3. Unit cells of NiAl in real and reciprocal spaces.

Energy-distribution curves (EDC's) as a function of photon energy taken normal to the (111) surface are displayed in Fig. 4. In this measurement the band structure from Γ to R is measured, i.e., the Λ bands (Fig. 1). An arrow indicates a peak in the EDC that is associated with a bulk band of Λ_1 (solid curve) or Λ_3 (dashed curve) symmetry. Hatched peaks are surface features associated with the (111) face.[38] The variations in energy positions of the Λ_1 and Λ_3 bulk peaks as a function of photon energies can be plotted to show the initial-state dispersions, and the binding energies of high-symmetry points can be determined directly.[27] The band structure along ΓR has been constructed from the photoemission data with the use of free-electron final bands.

Figures 5 and 6 depict the occupied band structure of NiAl obtained from photoemission data like those displayed in Fig. 4 for the high-symmetry directions. The dispersions shown are for the energy range of the occupied d-band region. Solid lines are the calculated bulk dispersions reproduced from Fig. 1. The values of the Γ_{12} and $\Gamma_{25'}$ symmetry points measured from three different crystals are found to be within ± 0.05 eV. The reproducibility of the data is strong evidence that the experimental procedure is correct.[27] In Fig. 6(a) two sets of symbols are used to separate data points collected by normal and off-normal emission.[27] The △, ○, and × denote data obtained from normal emission, while ▲, ●, and ■ denote data obtained from off-normal emission.

The measured and calculated binding energies at high-symmetry points are compared in Table II. The calculational results we have chosen for comparison with measurements include two muffin-tin schemes [augmented plane wave (APW) and Korringa-Kohn-Rostoker (KKR)], a recent pseudopotential scheme, and our full-potential schemes, all carried out to self-consistency. The first column in Table II gives the measured binding energies of the high-symmetry points. The error bounds represent several combined factors, including instrumental resolution, errors in assigning peak energies, and uncertainties in the determination of the Fermi level at higher photon energies ($\hbar\omega > 60$ eV). The second column presents energy eigenvalues from a 1977 APW band calculation by Nagel.[23] Column 3 presents the results of a

1988 pseudopotential band calculation by Kang.[39] Column 4 gives the band energies obtained from the 1974 KKR calculation of Moruzzi *et al.*[22] The last column presents eigenvalues obtained from our full-potential LASTO calculation. The comparisons between theory and experiment will be discussed in Sec. V and are summarized as follows.

(1) The overall agreement of photoemission measurements with results of full-potential band calculations for band dispersions are remarkably good. For example, the calculation closely reproduces the dispersion of the Σ_1 band from $\Gamma_{25'}$ to $M_{5'}$.

(2) More quantitative comparison shows a systematic discrepancy between theory and experiment. The measured dispersions of all the bulk bands displayed in Figs. 5 and 6 and the binding energies at high-symmetry points

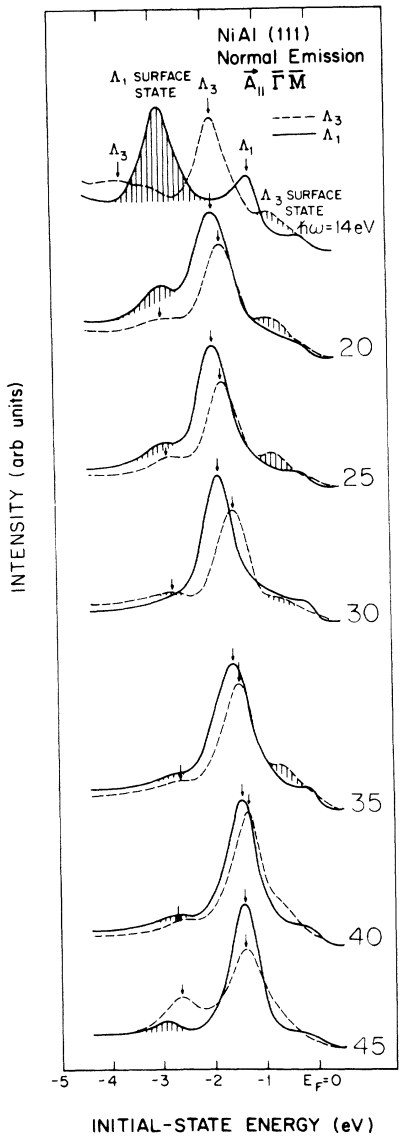

FIG. 4. Normal-emission photoemission spectra over the photon-energy range 14–45 eV. Dispersions of the Λ_1 and Λ_3 bulk bands are marked by arrows. Hatched peaks are surface states.

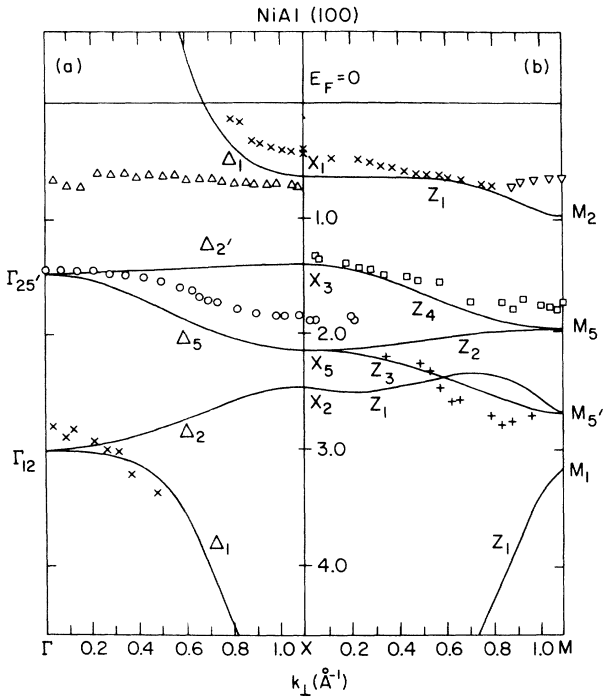

FIG. 5. Comparison between measured and calculated band dispersions along (a) ΓX and (b) XM.

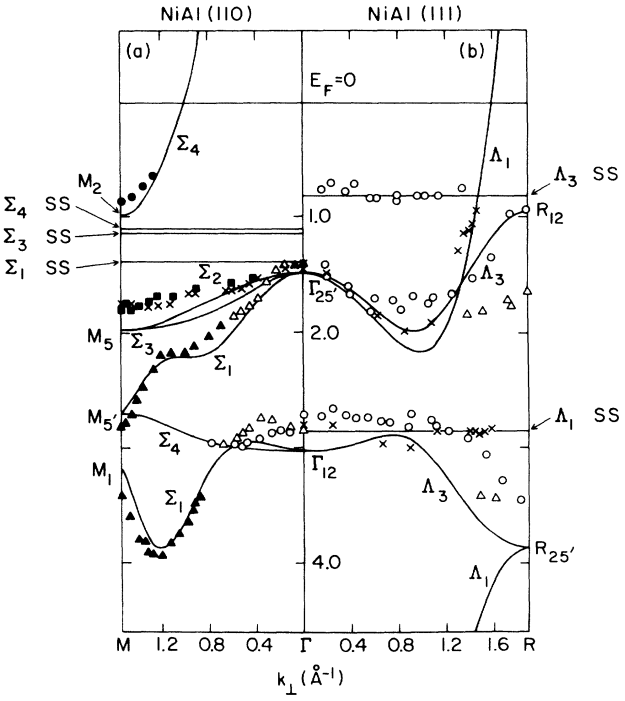

FIG. 6. Comparison between measured and calculated initial-state dispersions: (a) Along ΓM. △, ○, and × denote data obtained from normal emission from the Σ_1, Σ_4, and Σ_3 states, respectively, while ▲, ●, and ■ denote data obtained from off-normal emission from the Σ_1, Σ_4, and Σ_2 states, respectively. (b) Along ΓR. The ○'s denote data obtained from the Λ_3 state, while ×'s denote data obtained from the Λ_1 state. The △'s are not associated with any specific bands (see Ref. 27). Horizontal lines indicate energy positions of surface states.

are shallower than those obtained from the calculation. The differences between measurement and theory are due to many-body effects and can be treated as the real part of the self-energy (in fact this defines the self-energy). The comparison with Ni will be discussed in Sec. V.

(3) Intrinsic surface states with well-defined symmetry were found in both the (110) and (111) faces of NiAl. Their energy positions are indicated by horizontal lines drawn across the zone. Comparison between the measured and calculated surface band dispersions have been published elsewhere.[38,40] For the (100) face, however, a feature at -0.72 eV was found [indicated by Δ along ΓX in Fig. 5(a)], which is probably an extrinsic surface state without a well-defined symmetry.

B. Fermi-surface determination

The Fermi surface of NiAl has been obtained from band calculations by Nagel.[23] However, the shape of the Fermi surface has not been measured experimentally. In this subsection we present the projection of the Fermi surface of NiAl in a (100) plane of the bulk Brillouin zone measured by photoemission. Since the upper Δ_1 band (the seventh band) was found to have a strong transition across the Fermi level away from $\bar{\Gamma}$, we used this band to illustrate how we can measure the Fermi surface of a (100) plane.

To begin the measurement, the crystal was oriented such that $\mathbf{A}\|\bar{\Gamma}\bar{X}$ (see Appendix B). Using s-polarized light and moving the analyzer to the zone boundary ($\bar{X}$ of the SBZ), the transition of the Δ_1 band was found to be very strong at a photon energy of 16 eV. This photon energy was found to connect the initial state at X_1 to the final state at X_5. The EDC's in Fig. 7 show the dispersion of the Δ_1 band with $\mathbf{k}_\parallel$. The Δ_1 band has a binding energy of 0.50 eV at X_1 ($k_\parallel = 1.088$ Å^{-1}) and disperses up towards the Fermi level. The inset contains a plot of the dispersion of this free-electron-like band with $m^* = 1$. Moving the analyzer collection angle back towards $\bar{\Gamma}$, the Fermi-level crossing of the Δ_1 band was observed at $\mathbf{k}_\parallel = 0.74 \pm 0.02$ Å^{-1}. This measurement gives point A of the Fermi-surface cross section shown in Fig. 8. Owing

TABLE II. High-symmetry points in the NiAl band structure.

Symmetry points	Experimental value	APW (Nagel)[a]	Pseudopotential (Kang)[b]	KKR (Moruzzi)[c]	LASTO (this work)
Γ_1	11.0±0.20 (110)	10.87	11.12	10.88	10.74
Γ_{12}	2.72±0.10	3.29	3.19	3.38	3.02
$\Gamma_{25'}$	1.44±0.10	1.51	1.52	1.61	1.49
R_{12}	0.91±0.10 (111) 0.88±0.20 (100)	1.02	0.95	1.15	0.97
$R_{25'}$	3.50±0.15 (111)	3.99	4.04	4.04	3.88
M_2	0.85±0.20 (100)	1.05	0.97	1.18	1.00
M_5	1.75±0.15 (110) 1.76±0.10 (100)	2.02	2.06	2.11	1.98
$M_{5'}$	2.80±0.30 (100)	2.71	2.92	2.73	2.71
M_1	3.35±0.40 (100)	3.33	3.38	3.40	3.19
M_3		5.20	5.26	5.20	5.11
X_1	0.47±0.15 (111) 0.50±0.10 (100)	0.63	0.63	0.74	0.66
X_3	1.28±0.10 (100)	1.41	1.42	1.53	1.42
X_5	1.88±0.15 (111) 1.89±0.10 (100)	2.18	2.21	2.27	2.15
X_2	2.32±0.15 (111)	2.81	2.70	2.92	2.48
X_1		6.54	6.79	6.58	6.49
$X_{4'}$		6.75	6.97	6.74	6.70
$R_{12}-R_{25'}$	2.60	2.97	3.09	2.89	2.91
Δ_d%		14.2	18.8	11.2	11.9

[a]Reference 23.
[b]Reference 39.
[c]Reference 22.

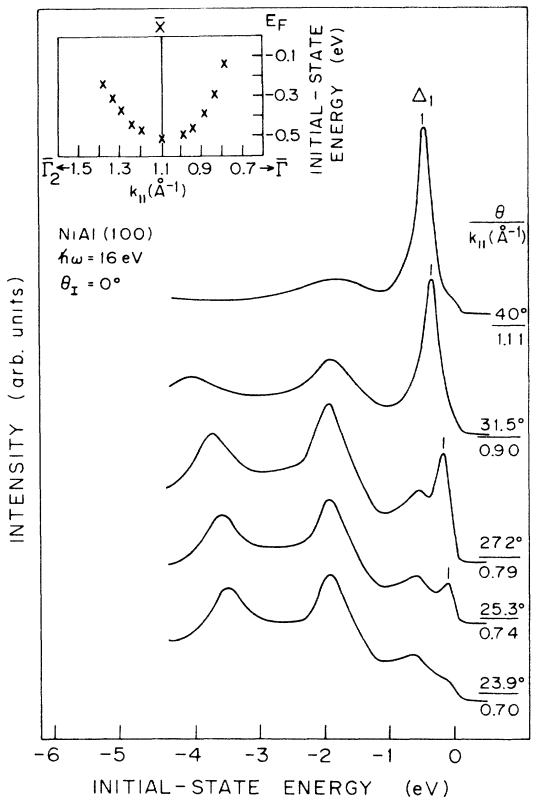

FIG. 7. Photoemission spectra as a function of $\mathbf{k}_{\parallel}$ showing the dispersion of the Δ_1 band. The inset shows that the dispersion of the Δ_1 band is free-electron-like with $m^*=1$.

to the high symmetry of the cubic Brillouin zone, we only need to determine the Fermi surface in $\frac{1}{8}$ of the zone, and the Fermi surface of the (100) plane can be generated by symmetry operations. In Fig. 8 the Fermi surface was determined by changing $\mathbf{k}_{\perp}$, i.e., by increasing the photon energy from 16 eV and by changing the analyzer collection angle slightly, such that we could follow the Fermi-level crossing as the photon energy was increased. Point B in Fig. 8 was found at $\hbar\omega=25$ eV. The $\mathbf{k}_{\perp}$ at this point is obtained by a simple relationship using the free-electron-band model,

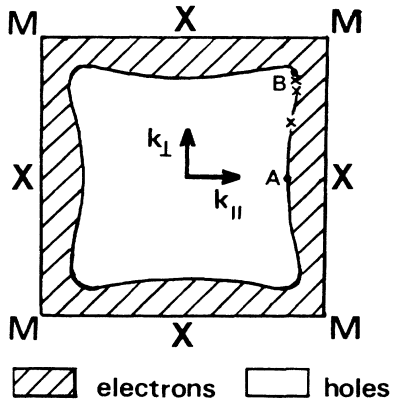

FIG. 8. Fermi-surface cross section of NiAl from the second zone. Electrons are filled around the perimeter and there is a hole pocket at the zone center.

$$\hbar\omega - E_i = \left[\frac{\hbar^2}{2m}\right]\mathbf{k}_{\parallel}^2 + \left[\frac{\hbar^2}{2m}\right](\mathbf{k}_{\perp}+\mathbf{G})^2 - V_0 \ , \qquad (3)$$

where V_0 is the inner potential. Since $E_i=0$ at the Fermi level and $\mathbf{k}_{\parallel}$ does not change appreciably from the previous value, Eq. (3) gives $\mathbf{k}_{\perp}=0.80\pm0.02$ Å^{-1} at point B. The Fermi cross section displayed in Fig. 8 is from the second zone since the Δ_1 band measured is an initial-state band folded back from the second Brillouin zone. The two-dimensional (2D) cross section of the Fermi surface in Fig. 8 shows a hole pocket at the center of the zone, with the occupied electron states in the hatched region. The measured Fermi surface obtained in this experiment is found to be in good agreement with that calculated by Nagel.[23]

V. DISCUSSION

A. Bandwidth

It is now accepted that there will be differences between the calculated band structure and that measured by photoemission. For example, the most famous case is Ni, where the experimental bandwidth is 30% narrower than the calculation.[2,6,7,41] The difference is due to the correlations between $3d$ electrons not included in the local-density approximation, and the fact that these calculation schemes are, in principle, restricted to the ground state. The magnitude of the discrepancy between theory and experiment for NiAl will indicate how important many-body effects are in this alloy system. A measure of the importance of these many-body effects can be obtained from the published data on Ni. If the d-band width is defined as the energy separation between the L_1 point[6] and the Fermi energy, then the experimental d-band width is $\sim$3.4 eV,[6] and theories predict $\sim$4.5 eV.[26,42] In NiAl the situation is slightly different in that the d band is filled. In order to facilitate a comparison of the bandwidth with Ni, the energy difference between R_{12} and $R_{25'}$ is used to define a d-band width in NiAl [see Figs. 1 and 6(b)]. Experimentally, the d-band width defined in this manner is 2.6 ± 0.25 eV, while the theoretical bandwidth is 2.9 eV. The discrepancy in NiAl is much smaller than in Ni.

The percentage of d-band narrowing, Δ_d, is calculated as

$$\Delta_d = \frac{\Delta E_c - \Delta E_m}{\Delta E_m}(100\%) \ , \qquad (4)$$

where $\Delta E_c = E_c(R_{25'}) - E_c(R_{12})$ and $\Delta E_m = E_m(R_{25'}) - E_m(R_{12})$.

E_c is the calculated eigenvalue of a high-symmetry point and E_m is the measured binding energy of that symmetry point. With this definition, Δ_d calculated for NiAl is given at the bottom of Table II for each theory. Both the full-potential and KKR calculations give a d-band narrowing of 12%. After discussing self-energy in the next subsection, we will return to this observation.

The d-band width can be estimated from the interatomic distances. According to the moment rules[34] dis-

cussed in Sec. II, the bandwidth of Ni is expected to be approximately 2.9 times larger than that of NiAl. A crude estimate from the density-of-states plot given in Sec. II is $W_{\mathrm{Ni}} \sim 5.6$ eV and $W_{\mathrm{NiAl}} \sim 2.9$ eV, leading to a ratio of 1.9. This suggests that the distance variation of t is less rapid than R^{-5}, and further suggests that hybridization between Ni d and Al p orbitals is important. Watson *et al.*[43] also quote reduction of the R^{-5} dependence for transition metals due to hybridization.

B. Self-energy

Photoemission measures the excitation spectra of the solid. The finite width of a spectral feature, its detailed shape, its overall strength, as well as its precise energy position are all influenced to varying degrees by dynamical interactions which are not contained in the independent-particle model. Because of the dynamical interactions between the hole left behind and the surrounding electrons in the excited state, the electronic structure of a periodic solid measured by photoemission is referred to as the "quasiparticle band structure." Therefore, a fully quantitative analysis of experimental data cannot be achieved solely on the basis of the one-electron picture, which is generally used to calculate the ground-state properties of solids. The corrections to the single-particle band structure due to these many-body effects are referred to as "self-energy" corrections.

Qualitatively, the difference between the measured and calculated band energies can be taken as a measure of the real part of the self-energy. Figure 9 shows a plot of the differences between the calculated high-symmetry-point energies (E_c) and the measured energies (E_m) as a function of E_m. In this figure, comparisons made with the full-potential calculation are indicated by symmetry labels such as Γ_{12}, $\Gamma_{25'}$, M_1, R_{12}, etc. Comparison with the APW and pseudopotential calculations are marked by symbols. The dashed line is an overlaid plot of $(E_c - E_m)/2$ versus E_m for pure Ni. The data for Ni are taken from Eberhardt and Plummer[2] and are compared to the theory of Wang and Callaway.[26] *Note that the results for Ni are scaled down by 60%.* Figure 9 shows that the discrepancy between theory and experiment follows the same trend for both Ni and NiAl. The largest derivation occurs around 3.0 eV in the d-band region. The important observations are the following. (1) The self-energy correction is considerably smaller in NiAl than in pure Ni. (2) This correction also has the same energy dependence. (3) The measured binding energy of the M_5 symmetry point is larger than that obtained from calculation, and $E_c - E_m$ is negative; this could be some interesting k-dependent self-energy, but is more likely an experimental problem. The first observation means that the d hole in NiAl is more delocalized and that the self-energy correction arising from the Coulomb interaction between two d holes is reduced. The delocalization of the d hole is a consequence of the following factors. (1) The d band of Ni is filled. In Ni the Fermi level falls into the region of high d density of states; the hole created by the excitation interacts with the holes in the unoccupied part of the d band.[10,44] This interaction leads to strong many-body effects and gives rise to the appearance of satellite structure in the Ni $3d$ valence band as measured by photoemission.[41,45] For NiAl the Ni d bands are filled. The probability of being in a two-hole final state is greatly reduced. This is consistent with the absence of satellite structure in the valence band[46] and a much weaker satellite structure in the core-level photoemission spectra of NiAl.[20,47] (2) The delocalized Al s,p electrons in NiAl can screen the d hole more effectively than in the case of pure Ni. (3) The p-d hybridization between the Ni d electrons and the Al s,p electrons makes the d electron less tightly bound to the Ni core, and the hole created by excitation is more delocalized. The combined effects of a filled Ni d band, additional screening by the Al s,p electrons, and p-d hybridization make the d hole in NiAl more delocalized and, consequently, the self-energy correction is reduced.

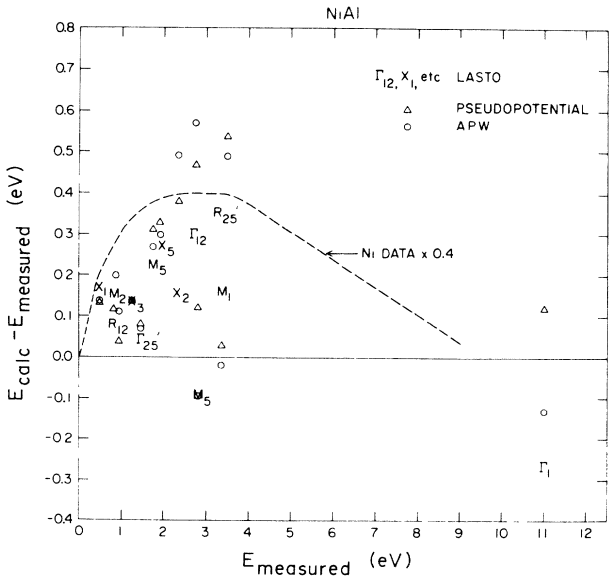

FIG. 9. Plot of the energy discrepancy $(E_c - E_m)$ as a function of the measured binding energy, E_m.

C. Lifetimes

The self-energy operator is a complex function. The real part produces a correction to the single-particle band dispersion and the imaginary part is the width of the spectral function. These two parts are intimately related. In this subsection we shall examine the imaginary part of the self-energy, i.e., the widths of the hole state (below the Fermi level) and the electron state (above the Fermi level).

In angle-resolved photoemission the widths of the observed interband transitions in $(E_i, \mathbf{k})$ are directly related to the widths of the corresponding hole and electron states. For an observed Lorentzian spectral distribution with a width Γ, the inverse hole and electron lifetimes as a result of the interband transition for normal emission are given by the following equation,[48]

$$\Gamma = \left| \frac{\Gamma_h + \Gamma_e |V_i / V_f|}{1 - V_i / V_f} \right| , \tag{5}$$

where $V_i = \partial E_i / \partial \mathbf{k}_\perp$ and $V_f = \partial E_f / \partial \mathbf{k}_\perp$ are the group velocities of the initial and final states perpendicular to the surface, E_i and E_f are initial- and final-state energies, and $\Gamma_h(E_i)$ and $\Gamma_e(E_f)$ are the full widths at half maximum (FWHM's) of the Lorentzian spectral distributions of the hole and electron states.

The energy broadening caused by the finite lifetime of an excited photoelectron can be estimated by measuring the intensity variation with photon energy for an initial state at the Fermi level. For $E_i = 0$ the hole-lifetime broadening Γ_h is zero and the electron inverse lifetime Γ_e can be measured directly from the FWHM of the resonant peak with $\hbar\omega$. To obtain an estimate of the electron inverse lifetime, Γ_e, a constant-initial-state (CIS) spectrum at the Fermi level ($E_i = 0$) was recorded from $\hbar\omega = 12$ to 47 eV for normal emission along the Δ symmetry line. Figure 10 shows that the Fermi-level crossings of the Δ_1 bands resonate at photon energies of 21 and 38.5 eV, corresponding to two free-electron-like final-state bands. After background subtraction, the two peaks in the CIS spectrum can be fitted with Lorentzian spectral functions. The FWHM was found to be 3.8 ± 0.2 and 6.1 ± 0.2 eV at $\hbar\omega = 21$ and 38.5 eV, respectively.

To estimate the average energy-dependent momentum broadening $\Delta\mathbf{k}(E)$, we need to know the average electron mean free path $l(E)$ since $\Delta\mathbf{k}$ is given as $\Delta\mathbf{k}(E) = 1/l(E)$. Using the relation $l(E) = (\partial E_f / \partial \mathbf{k}_\perp)/\Gamma_e(E)$, with $E_f = \frac{3.81}{1.089}(\mathbf{k}+\mathbf{G})^2 = 3.7$ [where $\mathbf{G} = (2\pi/a)(\bar{1},0,0)$ and $\mathbf{G} = (2\pi/a)(2,0,0)$, respectively, for the two final-state bands], we found that $\partial E_f / \partial \mathbf{k}_\perp \sim 20$ eV Å, for $\Gamma_e = 3.8$ eV and $\partial E_f / \partial \mathbf{k}_\perp \sim 25$ eV Å for $\Gamma_e = 6.1$ eV. Table III gives the values of $l(E)$ and $\Delta k(E)$ for NiAl.

In Fig. 11 the electron inverse lifetime (Γ_e) of NiAl is compared to other metallic elements [Mg (Ref. 49), Zn (Ref. 50), Al (Ref. 3), and Cu (Ref. 51)]. The two data points for NiAl are taken from the width of the Lorentzian spectral function in Fig. 10. Figure 11 shows that, qualitatively, electron-lifetime broadening is nearly the same for free-electron metals and for the alloy NiAl, although the electron lifetime of NiAl is slightly shorter.

A measure of the hole inverse lifetime (Γ_h) of NiAl is given in Fig. 12. Data points plotted in this figure are the measured peak widths from the photoemission spectra taken at high-symmetry points in the bulk Brillouin zone and with the instrumental functions taken out of each spectrum. The Γ_h is plotted against E/E_F to allow for comparison with the calculated imaginary part of the self-energy for an electron gas of Hedin using the RPA (random-phase approximation).[52] Data for Al (Ref. 3) and Ni (Ref. 2) are included for comparison. Since most of the symmetry points shown in Fig. 12 are in the *d*-band region, dispersions near Γ and near the zone boundaries are relatively flat. If we then make the assumption that V_i in Eq. (5) is zero, Eq. (5) can be simplified to give $\Gamma = \Gamma_h$. Near the X_1 point, the dispersion of the Δ_1 band is free-electron-like, and additional smearing from $\Delta k_\parallel$ is expected. This was reflected by a broader Gaussian function used to fit the Fermi level. The hole inverse lifetime of bulk states in NiAl is comparable to that of pure Al, which has approximately the same charge density (r_s). The data for NiAl can be fitted with a parabolic function that goes through zero at the Fermi level. Qualitatively, the damping of holes through Auger decay can be estimated from a phase-space argument since the number

TABLE III. Electron mean free path and averaged momentum broadening in NiAl.

$\Gamma_e(E)$ (eV)	$\partial E_f/\partial \mathbf{k}_\perp$ (eV Å)	E_f (eV)	$l(E)$ (Å)	$\Delta\mathbf{k}(E)$ (Å^{-1})
3.8	20	21	5.3	0.19
6.1	25	38.5	4.1	0.24

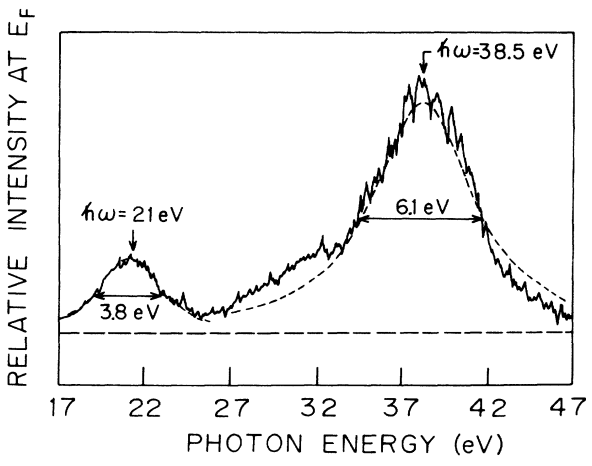

FIG. 10. Intensity of Fermi-energy electrons as a function of photon energy for normal emission.

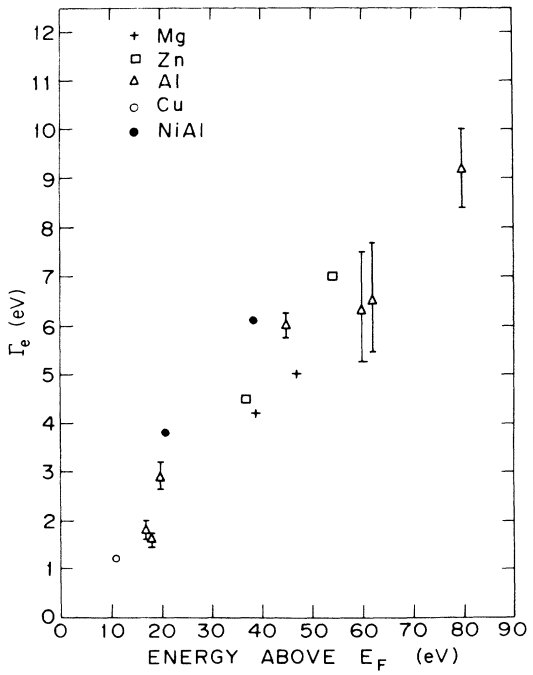

FIG. 11. Electron inverse lifetimes (Γ_e) for NiAl and other free-electron metals—Mg (Ref. 49), Zn (Ref. 50), Al (Ref. 3), and Cu (Ref. 51)—as a function of electron energy.

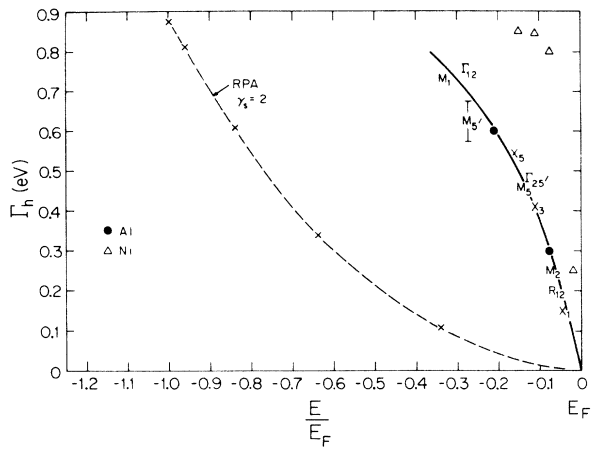

FIG. 12. Measured inverse hole lifetimes (Γ_h) for NiAl, Ni (Ref. 2), and Al (Ref. 3) plotted against E/E_F. The dashed curve is the prediction of the RPA calculated for an electron gas (Ref. 52) with $r_s = 2$.

of decay channels increase when the hole is further away from the Fermi level. In the Auger-decay process, the probability of a hole being filled near the Fermi level is $\approx [N(E_F)\Delta E]^2$, where $N(E_F)$ is the density of states at the Fermi level and ΔE is the energy of the hole with respect to the Fermi level.

The dashed curve shown in Fig. 12 is the prediction by Hedin[52] calculated for an electron gas with $r_s = 2$. A comparison of the measured and calculated hole lifetimes shows a very large discrepancy, which should not be surprising since the real part of the self-energy calculated using the RPA does not agree with experiment. What is surely needed at the present time is a procedure capable of calculating both the real and the imaginary parts of self-energy including the band structure of the solid.

D. Core-level shifts and charge transfer

We have measured the core-level binding energies for Ni, Al, and NiAl. The values are given in Table IV, where it can be seen that as a rule the Ni core levels shift to larger binding energy while the aluminum core levels shift to smaller binding energy. As discussed in the Introduction, this is opposite to what might have been expected using simple electronegativity arguments. In order to study these shifts, we compare the measured and calculated binding energies of the Ni and Al core levels in NiAl, Ni, and Al.

The binding energies of the core levels were measured by x-ray photoelectron spectroscopy (XPS). We have measured both the Ni and Al core levels in pure Ni and Al and the same core levels for NiAl. Figure 13 shows two photoemission spectra of the Ni $2p_{3/2}$ core level, one from pure Ni and one from NiAl. The difference in the binding energies (core-level shift, ΔE_B) of the two peaks is 0.5±0.1 eV, the binding energy of the Ni $2p_{3/2}$ core level in NiAl being larger. A comparison of the core-level binding energies between NiAl and Al shows that the Al $2p_{3/2}$ core level in NiAl is 0.2 eV smaller in binding energy than in Al.

Theoretically, core-level positions are often partitioned into initial- and final-state shifts. The initial-state shifts (which are not measurable) are calculated using wave functions appropriate for the ground state (i.e., not allowing any final-state relaxation). It has been shown (see Ref. 53) that the initial-state shifts are given approximately by the shift in the core-level eigenvalue ε_i. The magnitudes of these ε's (relative to the Fermi energy) are also given in Table IV. It can be seen that the changes in binding energy from the pure metallic element to the compound agree reasonably well with experiment (and all have the correct sign), but the magnitude has a large error. We attribute the error both to neglect of final-state relaxation and to errors in the local-density approximation itself.[54]

Shifts to larger binding energy are usually interpreted as resulting from electron transfer away from a site. Therefore the core-level shifts can be understood to imply electron transfer from nickel to aluminum. This is interesting because the Pauli electronegativity of Ni is greater than that of Al, which would suggest electron

TABLE IV. Measured and calculated core-level shifts (in eV) for NiAl.

	Ni core levels					
	NiAl		Ni		ΔE_B[b]	
	Theor.[a]	Expt.	Theor.	Expt.	Theor.	Expt.
$3p_{3/2}$	62.6	66.9±0.1	62.3	66.5±0.1	+0.3[c]	+0.4
$2p_{3/2}$	830.1	853.3±0.1	829.9	852.8±0.1	+0.2	+0.5
$2p_{1/2}$	847.5	870.5±0.1	847.3	870.3±0.1	+0.2	+0.2
	Al core levels					
	NiAl		Al		ΔE_B	
	Theor.[a]	Expt.	Theor.	Expt.	Theor.	Expt.
$2p_{3/2}$	64.2	72.7±0.1	64.7	72.9±0.1	−0.5	−0.2
$2s$	102.2	117.6±0.1	102.7	117.9±0.1	−0.5	−0.3

[a]Kohn-Sham eigenvalues—present calculation.
[b]$\Delta E_B = E_B(\text{NiAl}) - E_B(\text{Ni or Al})$.
[c]For reference to other calculations, this number is +0.26.

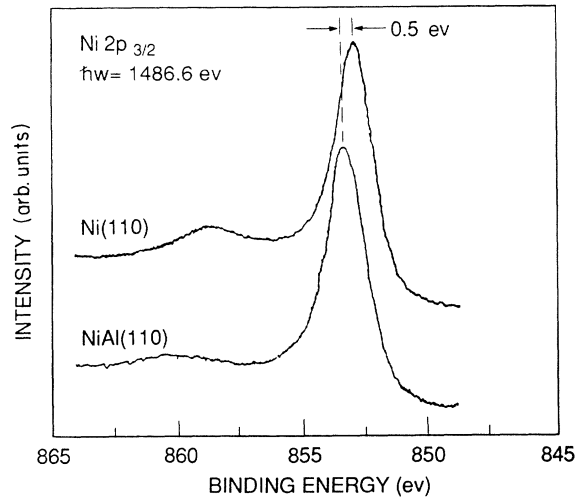

FIG. 13. XPS spectra of the Ni $2p_{3/2}$ core level in Ni and in NiAl.

transfer to Ni. Also, the usual picture of the bonding in these materials[55] involves strong overlap of Ni d with Al p orbitals and a concomitant filling of the hybridized "d" band with, again, electron transfer to Ni.

Our calculations support the idea that electrons are transferred to Al, although it is always difficult to quantify charges because they are not precisely defined quantities.[56] One measure of charge transfer that is well defined is the charge inside the muffin-tin spheres. By this measure both Ni and Al gain about $0.1e^-$. The problem is that there is almost $2e^-$ worth of charge in the interstitial region and there is no unique way of assigning that charge to one site or the other. We have previously used two separate measures of this interstitial charge—the Wigner-Seitz charge and a Mulliken-population analysis. The Wigner-Seitz charge is obtained by expanding the muffin-tin spheres slightly so that their total volume is equal to the volume of the unit cell. The charge density is smoothly extrapolated from inside these muffin-tin spheres and integrated. In this way we obtain Δn (the change in charge) for Al of $+0.15e^-$ (and $-0.15e^-$ for Ni). In this analysis the Ni gains d electrons but loses more sp electrons. The changes in Mulliken population show the same trend, but the numbers are an order of magnitude larger. For Al, Δn is $+1.1e^-$ (and $-1.1e^-$ for the Ni) and, again, the Ni gains $\sim 0.1d$ electron but loses ~ 1.2 sp electrons.

We do not regard the actual value of the charge transfer as significant, but instead we take the sign of the total and d-electron transfer as being consistent with the filling of the d band and the shift of the nickel core levels to larger binding energy. We also note that cluster calculations and some band-structure calculations have been interpreted to imply charge transfer in the opposite direction, i.e., from Al to Ni.[57,58] Compensating s- and d-electron transfer has been found previously in gold alloys,[59] but there the d electrons dominate the core-level shift, and the net charge transfer is in the direction predicted by electronegativity.

E. p-d hybridization

As mentioned previously, the standard picture of bonding in NiAl relies heavily on the coupling between Ni d states and Al p states.[55] To illustrate this hybridization, we have calculated the energy bands along the [111] direction (Γ to R) with the matrix elements of the Hamiltonian and overlap which couple the d states to the sp

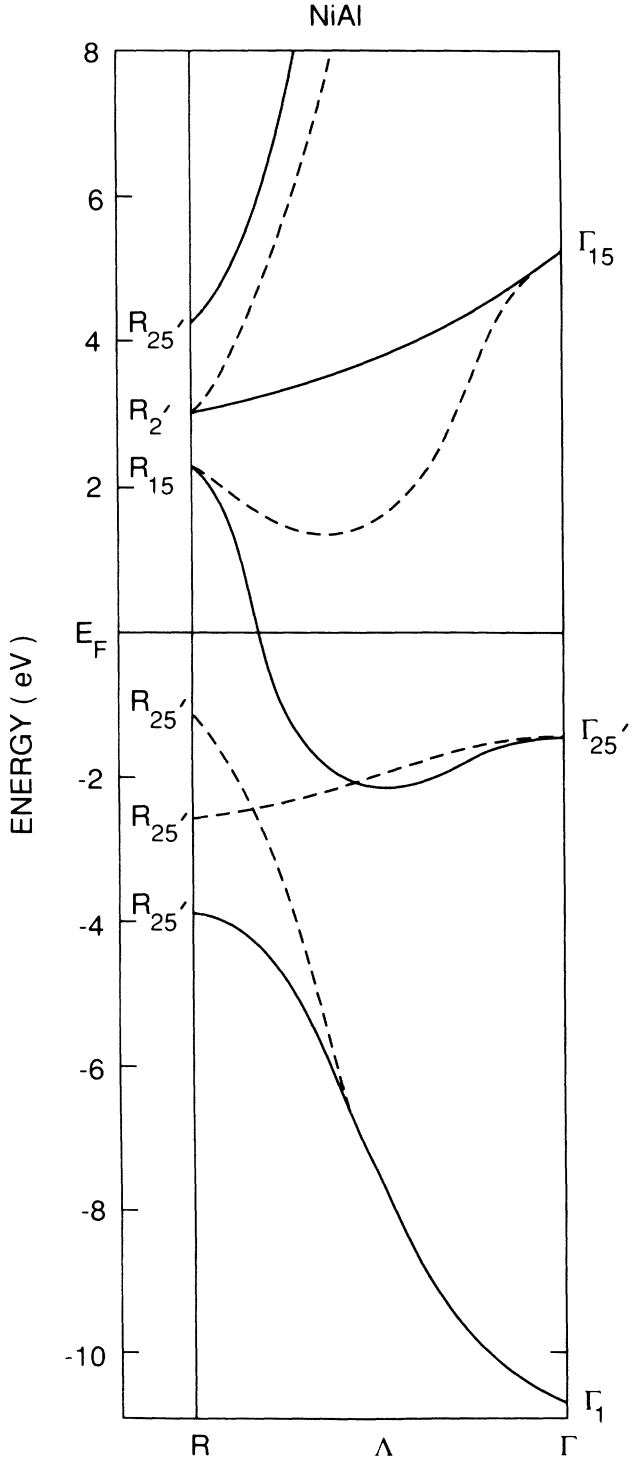

FIG. 14. Calculated energy bands along Γ and R (solid curves) and with d hybridization set to zero (dashed curves).

states set to zero. It is one of the advantages of the LASTO method that the bands are eigenvalues of a Hamiltonian that is labeled by site- and angular-momentum (s, p, d, etc.) indices. The solid curves in Fig. 14 show the energy bands calculated in the usual way (the same as in Fig. 1). The dashed curves show the bands with d hybridization turned off. At the R point the state at -1.1 eV is pure Al p, while that at -2.5 eV is pure Ni d. When the coupling is turned on, these levels interact and the state at -3.9 eV has a Mulliken population of 67% Ni d and 33% Al p. The "antibonding state" that has been pushed above the Fermi level to $+4.3$ eV is 35% Ni d and 65% Al p. It can be seen from the figure that the largest degree of mixing occurs at R. The bands in other parts of the zone are relatively less affected. This illustrates the importance of p-d bonding in this alloy system.

VI. CONCLUSION

We have presented a detailed experimental and theoretical picture of the electronic structure of NiAl. We find a filled "d" band with a relatively low density of states at the Fermi level (about twice that of pure aluminum, but only $\frac{1}{5}$ that of pure nickel). We find that the band structure as determined by angle-resolved photoemission is in relatively good agreement with our state-of-the-art local-density calculations. For example, the error in the calculated bandwidth is about 12% (calculation too large), as compared with more than 30% for pure nickel. This is in spite of the fact that the d band is narrower in NiAl than in pure Ni, which might have led one to expect greater errors in the local-density calculations (narrower bands are harder to describe in a band theory). We attribute this to the fact that the bands, though narrower, are filled, and band theories work well for filled bands.

We have found significant Ni d–Al p hybridization and have illustrated this by giving the energy bands from Γ to R with the p-d-hybridization terms set to zero.

We have also measured the core-level shifts, which are positive for nickel (greater binding energy) and negative for aluminum. This was correlated with electron transfer from nickel to aluminum (opposite to electronegativity). Furthermore, the electron transfer was predominantly among the sp electrons. The d states showed increased electron count, as expected from the simple p-d-bonding picture.[55]

ACKNOWLEDGMENTS

We wish to acknowledge many useful discussions with R. E. Watson and M. Weinert. This research was supported in part at the University of Pennsylvania by the U.S. National Science Foundation through the Materials Research Laboratories Program under Grant No. DMR-88-19885 and by the Division of Materials Sciences, U.S. Department of Energy, under Contract No. DE-AC02-76CH00016, and by the Division of Materials Sciences, U.S. Department of Energy, under Contract No. DE-AC05-84OR21400 with Martin Marietta Energy Systems, Inc.

APPENDIX A: DISPERSION OF THE OCCUPIED BANDS

The band dispersion is measured by use of angle-resolved photoemission and the data are analyzed based on the direct-transition model and simple symmetry selection rules using the polarization of the incoming radiation from the storage ring. The polarization selection rules can easily be understood from the photoemission matrix element in the dipole approximation,

$$M_{fi} \propto |\mathbf{A}\cdot\langle\psi_f(\mathbf{k}_f)|\mathbf{P}|\psi_i(\mathbf{k}_i)\rangle|^2 . \quad \text{(A1)}$$

ψ_f and ψ_i are the final- and initial-state wave functions, $\mathbf{A}$ is the vector potential of the light, and $\mathbf{P}$ is the momentum operator. For emission normal to the surface, the detected plane-wave final state is totally symmetric under point-group operations about the surface normal. The symmetry of the initial state is then the same as that of the dipole operator causing the optical transition; i.e., if ψ_f is even, $\mathbf{A}\cdot\mathbf{P}|\psi_1\rangle$ must also be even in order to observe any intensity in the detector. In other words, for an allowed transition the unity representation must be contained in the direct product of the representations of the initial state, the final state, and the dipole operator.[60] Using the known final-state symmetry, the dipole-allowed initial states for normal emission from low-index faces of NiAl are listed in Table V. In this table the polarization direction is referred to a coordinate system specified by a set of orthogonal axes x,y,z in which the z axis is normal to the surface plane.

At the $\bar{\Gamma}$ point, the initial states of the NiAl system have the full point-group symmetry as given in Table V. Away from $\bar{\Gamma}$, the symmetry of the initial states is reduced and the wave function of each initial state can be discussed as having either even or odd *reflection* symmetry with respect to a surface mirror plane. The symmetry selection rule has been discussed in Ref. 61.

In NiAl the Ni d electrons are characterized by one of the five d wave functions: d_{z^2}, $d_{x^2-y^2}$, d_{xz}, d_{yz}, and d_{xy}. If we use an orthogonal set of axes x,y,z, with z being the surface normal and x,y lying in the surface plane, the d_{z^2} wave function is even with respect to reflection about both the yz and xz planes. An initial state with d_{xz} (d_{yz}) character is even with respect to the xz (yz) plane and odd with respect to the yz (xz) plane. For the d_{xy} and $d_{x^2-y^2}$ orbitals, which are both confined in the surface plane, the reflection symmetries with respect to both the xz and yz planes are odd for d_{xy} and even for $d_{x^2-y^2}$. Table VI gives the reflection symmetry of the initial-state bands away from $\bar{\Gamma}$ for the NiAl system.

Bulk photoemission can be viewed as a $\mathbf{k}$-conserving "direct-transition" process. As the photoelectron exits through the surface, the momentum component parallel to the surface, $\mathbf{k}_\parallel$, is conserved. The normal momentum $\mathbf{k}_\perp$ is changed during the exit since the electron has to escape from the solid. In the photoemission process, the initial- and final-state electron energies are related by

$$E_f = E_i + \hbar\omega . \quad \text{(A2)}$$

However, the energy measured by the detector is the ki-

TABLE V. Dipole-allowed initial-state symmetries for normal emission from the (100), (110), and (111) faces of NiAl in real and reciprocal spaces.

Real space							
Crystal face	Coordinate axes x	y	z	Irreducible representations	Initial-state symmetries $\mathbf{A}_\parallel x$	$\mathbf{A}_\parallel y$	$\mathbf{A}_\parallel z$
(100)	⟨100⟩	⟨010⟩	⟨001⟩	$\Delta_1,\Delta_{1'},\Delta_2,\Delta_{2'},\Delta_5$	Δ_5	Δ_5	Δ_1
(110)	⟨1$\bar{1}$0⟩	⟨001⟩	⟨110⟩	$\Sigma_1,\Sigma_2,\Sigma_3,\Sigma_4$	Σ_4	Σ_3	Σ_1
(111)	⟨$\bar{1}$10⟩	⟨$\bar{1}\bar{1}$2⟩	⟨111⟩	$\Lambda_1,\Lambda_2,\Lambda_3$	Λ_3	Λ_3	Λ_1
Reciprocal space							
Crystal face	Surface Brillouin zone x	y		Surface normal	Initial-state symmetries $\mathbf{A}_\parallel x$	$\mathbf{A}_\parallel y$	$\mathbf{A}_\parallel z$
(100)	$\bar{\Gamma}\bar{X}$	$\bar{\Gamma}\bar{X}$		z	Δ_5	Δ_5	Δ_1
(110)	$\bar{\Gamma}\bar{X}$	$\bar{\Gamma}\bar{Y}$		z	Σ_4	Σ_3	Σ_1
(111)	$\bar{\Gamma}\bar{M}$	$\bar{\Gamma}\bar{K}$		z	Λ_3	Λ_3	Λ_1

netic energy ($E_{\rm kin}$) of the photoelectron in vacuum. The purpose of the photoemission experiment is to determine the energy and momentum of the initial state from the measured energy and momentum of the emitted photoelectron. Since $\mathbf{k}_\parallel$ is conserved across the solid-vacuum interface, we can write the following equations for a given collection angle, θ_c, of the angle-resolved detector:

$$\mathbf{k}_\parallel(\text{outside})=\mathbf{k}_\parallel(\text{inside})+\mathbf{g}_\parallel\ , \tag{A3}$$

$$|\mathbf{k}_\parallel|(\text{Å}^{-1})=\left[\frac{2m}{\hbar^2}E_{\rm kin}(\text{eV})\right]^{1/2}\sin\theta_c\ . \tag{A4}$$

The perpendicular momentum component $\mathbf{k}_\perp$, is not conserved when the electron crosses the solid-vacuum interface, and can be determined only if the dispersion of the final-state band is known. The simplest approximation for the final state (E_f,k_f) is a parabolic free-electron-like band in a constant inner potential V_0,

$$E_f(\mathbf{k})=\frac{\hbar^2\mathbf{k}^2}{2m^*}-V_0\ , \tag{A5}$$

where $\mathbf{k}^2=\mathbf{k}_\parallel^2+\mathbf{k}_\perp^2$, m^* is the effective mass, and V_0 is the inner potential.

TABLE VI. Symmetry of the initial-state bands of NiAl.

Off-normal emission		
(100) face $\mathbf{A}_\parallel$	Symmetry of the initial-state bands Even	Odd
$\bar{\Gamma}\bar{X}$	Z_1,Z_3	Z_2,Z_4
$\bar{\Gamma}\bar{M}$	S_1,S_3	S_2,S_4
	Σ_1,Σ_3	Σ_2,Σ_4
	$T_1,T_{2'},T_5$	$T_2,T_{1'},T_5$
(110) face $\mathbf{A}_\parallel$	Symmetry of the initial-state bands Even	Odd
$\bar{\Gamma}\bar{Y}$	Δ_1,Δ_5	$\Delta_2,\Delta_{2'},\Delta_5$
	S_1,S_3	S_2,S_4
	$T_1,T_{2'},T_5$	$T_2,T_{1'},T_5$

Assuming a free-electron final band structure, the magnitude of $\mathbf{k}_\perp$ can be calculated according to

$$|\mathbf{k}_\perp|=\left[\frac{2m}{\hbar^2}(E_{\rm kin}+V_0+\phi)-|\mathbf{k}_\parallel|^2\right]^{1/2}\ , \tag{A6}$$

where ϕ is the work function. The assumptions of free-electron final bands were shown to work very well for Cu,[62] Ni,[7] and for NiAl as well.

APPENDIX B: SURFACE AND BULK BRILLOUIN ZONES

The surface Brillouin zones of the three low-index faces of NiAl are presented with respect to the bulk Brillouin zone. The high-symmetry points are vectors of the form

$$\Gamma X=(0,0,1)(\pi/a)=1.088\ \text{Å}\ ,$$

$$\Gamma M=(1,1,0)(\pi/a)=1.539\ \text{Å}\ ,$$

$$\Gamma R=(1,1,1)(\pi/a)=1.885\ \text{Å}\ .$$

The (100) SBZ is shown in Fig. 15, where

$$\bar{\Gamma}\bar{X}=\pi/a=1.088\ \text{Å}\ ,$$

$$\bar{\Gamma}\bar{M}=\sqrt{2}(\pi/a)=1.539\ \text{Å}\ .$$

The (110) SBZ is shown in Fig. 16, and the high-symmetry points $\bar{X}$ and $\bar{Y}$ of the surface are

$$\bar{\Gamma}\bar{X}=(1/\sqrt{2})(\pi/a)=0.769\ \text{Å}\ ,$$

$$\bar{\Gamma}\bar{Y}=\pi/a=1.088\ \text{Å}\ .$$

Figure 17 shows the (111) SBZ; the symmetry points of the surface are

$$\bar{\Gamma}\bar{M}=\frac{\pi}{\sqrt{2}a\cos 30^\circ}=0.889\ \text{Å}\ ,$$

$$\bar{\Gamma}\bar{K}=\frac{\pi}{\sqrt{2}a\cos^2 30^\circ}=1.026\ \text{Å}\ .$$

The designation of $\bar{M}_+$ and $\bar{M}_-$ in Fig. 17 is discussed

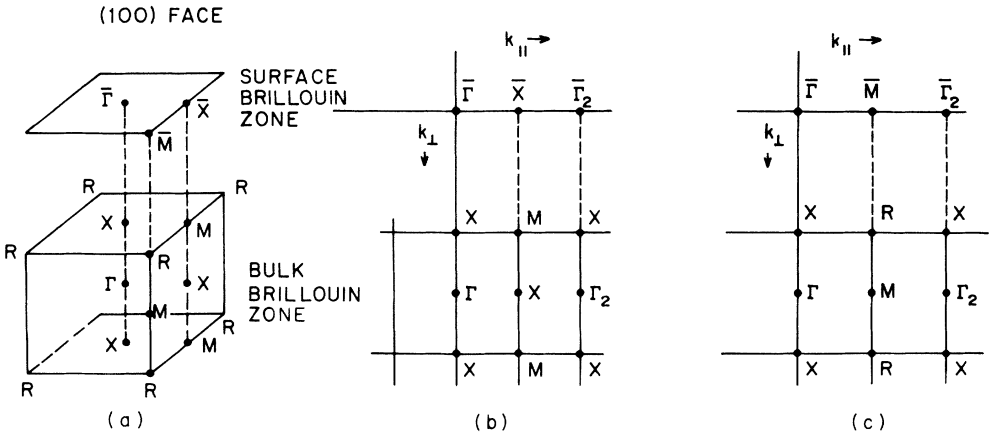

FIG. 15. Surface Brillouin zone (SBZ) for the (100) surface of NiAl compared to the bulk Brillouin zone. (a) SBZ with respect to the bulk Brillouin zone. (b),(c) Cuts through the bulk Brillouin zone along $\bar{\Gamma}\,\bar{X}$ and $\bar{\Gamma}\,\bar{M}$. $\mathbf{k}_{\parallel}$ is horizontal, $\mathbf{k}_{\perp}$ is vertical.

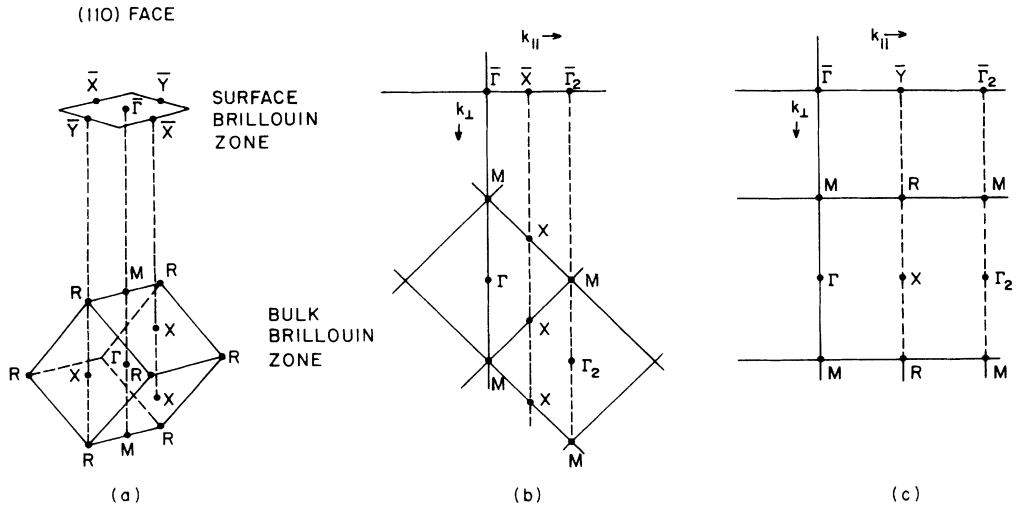

FIG. 16. Surface Brillouin zone (SBZ) for the (110) surface of NiAl compared to the bulk Brillouin zone. (a) SBZ with respect to the bulk Brillouin zone. (b),(c) Cuts through the bulk Brillouin zone along $\bar{\Gamma}\,\bar{X}$ and $\bar{\Gamma}\,\bar{Y}$. $\mathbf{k}_{\parallel}$ is horizontal, $\mathbf{k}_{\perp}$ is vertical.

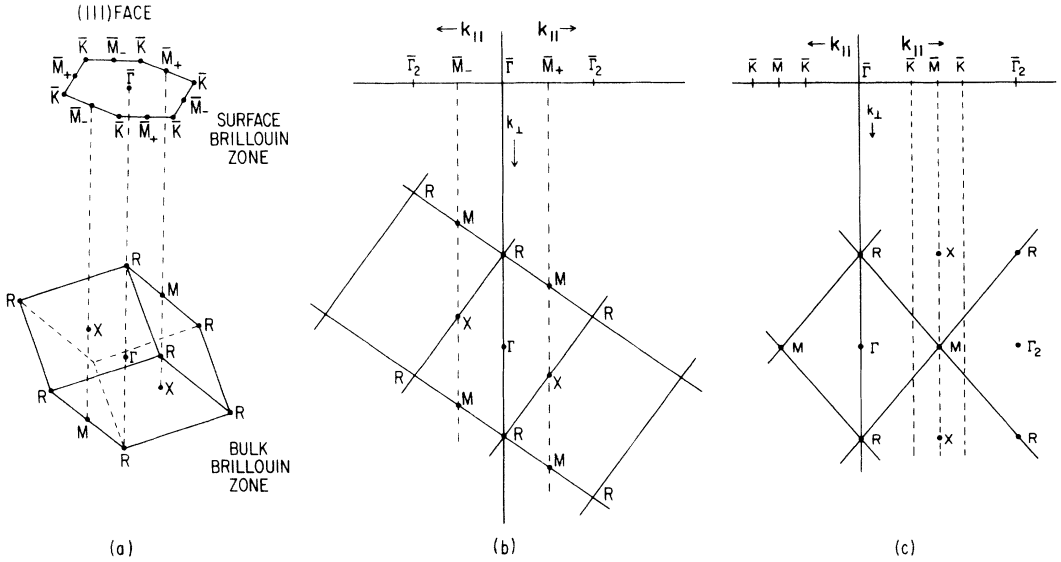

FIG. 17. Surface Brillouin zone (SBZ) for the (111) surface of NiAl compared to the bulk Brillouin zone. (a) SBZ with respect to the bulk Brillouin zone. (b),(c) Cuts through the bulk Brillouin zone along $\bar{\Gamma}\,\bar{M}$ and $\bar{\Gamma}\,\bar{K}$. $\mathbf{k}_{\parallel}$ is horizontal, $\mathbf{k}_{\perp}$ is vertical.

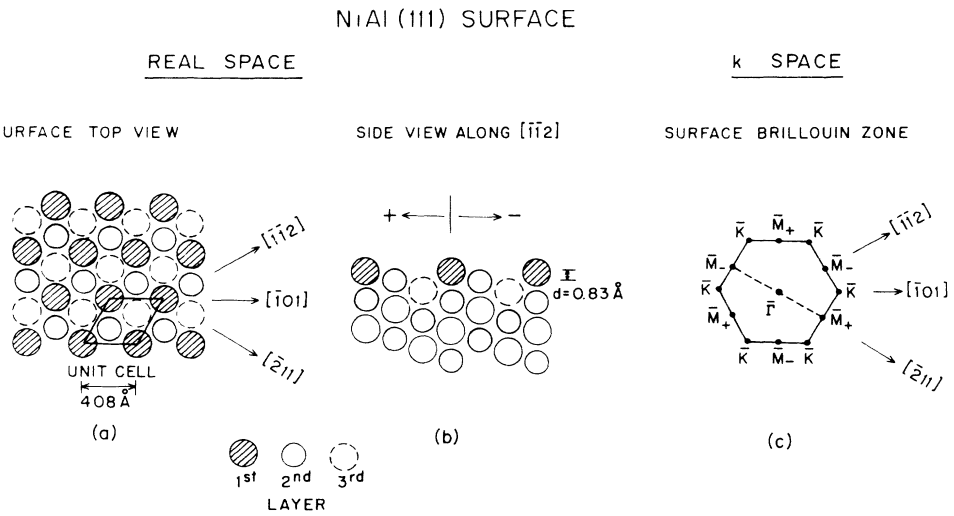

FIG. 18. Real- and reciprocal-space representations of the NiAl(111) surface. (a) Top view of an ideal (111) surface. (b) Side view along the $[\bar{1}\,\bar{1}\,2]$ direction. (c) Surface Brillouin zone showing the two inequivalent $\bar{M}$ points.

in the following.

The (111) surface Brillouin zone is hexagonal with sixfold symmetry. However, as one moves into the bulk along the [111] direction, the symmetry is reduced to only threefold. This is illustrated in Fig. 18(a). The (111) face of NiAl is an open surface; the two-dimensional unit cell is shown as a parallelogram in Fig. 18(a). Within the 2D unit cell, the first three layers of surface atoms are exposed. Figure 18(b) shows that, along the $[\bar{1}\,\bar{1}\,2]$ direction, the atomic arrangement of the first three layers in the positive and negative directions are not equivalent. Thus, the two $\bar{M}$ points in the SBZ are not the same with respect to the bulk Brillouin zone, and the symmetry is reduced to threefold. This is illustrated in Fig. 18(c). In our convention the two nonequivalent $\bar{M}$ points are designated $\bar{M}_+$ and $\bar{M}_-$, as determined from our bulk-band measurements.[27] $\bar{\Gamma}\bar{M}_+$ is along the $[\bar{2}11]$, $[1\bar{1}2]$, and $[1\bar{2}1]$ directions, while $\bar{\Gamma}\bar{M}_-$ is along the $[2\,\bar{1}\,\bar{1}]$, $[\bar{1}\,\bar{1}\,2]$, and the $[\bar{1}2\bar{1}]$ directions. Along the [110] direction, however, the atomic arrangements in either the positive or negative directions are the same. Thus, all six $\bar{K}$ points in the SBZ are equivalent.

APPENDIX C: SPIN-ORBIT SPLITTING

Spin-orbit splitting is usually neglected in the $3d$ elements; however, it can be important. In order to estimate the size of the spin-orbit splitting, it is useful to consider a simple tight-binding model of the d band supplemented by the spin-orbit interaction. The Hamiltonian can be written

$$H = H_{\mathrm{TB}} + H_{\mathrm{s.o.}} \ . \tag{C1}$$

The explicit form of the matrices is given, for example, in Ref. 30. In the limit of no spin-orbit splitting and for a cubic system, the eigenvalues are

$$\lambda = \begin{cases} 4p \ \ (\Gamma_{25'}) \ , \\ -6p \ \ (\Gamma_{12}) \ ; \end{cases} \tag{C2}$$

that is, one threefold- and one twofold-degenerate state. Upon comparison with our band calculation, where the splitting at Γ is $3.01-1.49=1.52$ eV, we obtain the parameter $10p=1.52$ eV.

In the absence of band-structure effects, the eigenvalues are those of $H_{\mathrm{s.o.}}$, which are

$$\lambda = \begin{cases} \xi, & j=\frac{5}{2} \\ -\frac{3}{2}\xi, & j=\frac{3}{2} \ ; \end{cases} \tag{C3}$$

that is, an atomic level with a spin-orbit splitting:

$$\Delta_{\mathrm{atom}} = \tfrac{5}{2}\xi \ . \tag{C4}$$

For nickel atoms $\Delta=0.28$ eV, so $\xi=0.11$ eV. For small ξ the combined Hamiltonian can be diagonalized using perturbation theory to yield

$$\lambda = \begin{cases} 4p+\xi \ \ (\Gamma_{7^+}) \ , \\ 4p-\xi/2 \ \ (\Gamma_{8^+}) \ , \\ -6p \ \ (\Gamma_{7^+}) \ ; \end{cases} \tag{C5}$$

therefore the spin-orbit splitting of the $\Gamma_{25'}$ level is just

$$\tfrac{3}{2}\xi = \tfrac{3}{5}\Delta_{\mathrm{atom}} = 0.17 \text{ eV} \ . \tag{C6}$$

Experimentally, we did not observe the spin-orbit splitting at $\Gamma_{25'}$. This is due to lifetime broadening (see Fig. 12), which, for levels near -1.5 eV, is of the order of 0.5 eV. This broadening prevents us from observing the spin-orbit splitting, which is only 0.17 eV.

[1]R. Hultgren, P. D. Desai, D. T. Hawkins, M. Gleiser, and K. K. Kelley, *Selected Values of the Thermodynamic Properties of Binary Alloys* (American Society for Metals, Metals Park, OH, 1973).
[2]W. Eberhardt and E. W. Plummer, Phys. Rev. B **21**, 3245 (1980).
[3]H. J. Levinson, F. Greutter, and E. W. Plummer, Phys. Rev. B **27**, 727 (1983).
[4]V. Heine, in *The Physics of Metals,* edited by J. M. Ziman (Cambridge University Press, Cambridge, 1969).
[5]J. Friedel, in *The Physics of Metals* (Ref. 4).
[6]D. E. Eastman, F. J. Himpsel, and J. A. Knapp, Phys. Rev. Lett. **40**, 1514 (1978).
[7]F. J. Himpsel, J. A. Knapp, and D. E. Eastman, Phys. Rev. B **19**, 2919 (1979).
[8]C. Guillot, Y. Ballu, J. Paigne, J. Lecante, K. P. Jain, P. Thiry, R. Pinchaux, Y. Petroff, and L. M. Falicov, Phys. Rev. Lett. **39**, 1632 (1977).
[9]S. Hüfner, and G. K. Wertheim, Phys. Lett. **51A**, 299 (1975); **51A**, 301 (1975).
[10]D. R. Penn, Phys. Rev. Lett. **42**, 921 (1979).
[11]P. Heller, Rep. Progr. Phys. **30**, 731 (1967).
[12]J. A. Seitchik and R. H. Walmsley, Phys. Rev. **131**, 1473 (1963); J. J. Spokas, C. H. Sowers, D. O. Van Ostenburg, and H. G. Hoeve, Phys. Rev. B **1**, 2523 (1970).
[13]F. De Boer, J. Biesterbos, and C. J. Schinkel, Phys. Lett. **24A**, 335 (1967); F. R. De Boer, C. J. Schinkel, J. Biesterbos, and S. Proost, J. Appl. Phys. **40**, 1049 (1969).
[14]B. I. Min, A. J. Freeman, and A. F. Jansen, Phys. Rev. B **37**, 6757 (1988).
[15]F. Seitz, *The Modern Theory of Solids* (McGraw-Hill, New York, 1940), Chap. 8.
[16]P. O. Nilsson, Phys. Status Solidi **41**, 317 (1970).
[17]A. P. Kawolczyk, G. Apai, G. Kaindl, F. R. McFeely, L. Ley, and D. A. Shirley, Solid State Commun. **25**, 847 (1978).
[18]W. Blau, J. Weisbach, G. Merz, and K. Kleinstück, Phys. Status Solidi B **93**, 713 (1979).
[19]S. B. Maslenkov, A. I. Kozlenkov, S. A. Filin, and A. I. Shulgin, Phys. Status Solidi B **123**, 605 (1984).
[20]John C. Fuggle, F. Ulrich Hillebrecht, R. Zeller, Zygmunt Zołnierek, and Peter A. Bennett, Phys. Rev. B **27**, 2145 (1983).
[21]J. W. D. Connolly and K. H. Johnson, in *Electronic Density of States,* edited by L. H. Bennett, Nat. Bur. Stand. (U.S.) Spec. Publ. No. **323**, Washington, D. C. (U.S. GPO, 1971), p. 19.
[22]V. L. Moruzzi, A. R. Williams, and J. F. Janak, Phys. Rev. B **10**, 4856 (1974).
[23]David J. Nagel, Ph.D. thesis, University of Maryland, 1977.
[24]C. H. Muller, H. Wonn, W. Blau, P. Ziesche, and V. P. Krivitskii, Phys. Status Solidi B **95**, 215 (1979).
[25]L. Pauling and P. Pauling, *Chemistry* (Freeman, San Francisco, 1975).
[26]C. S. Wang and J. Callaway, Phys. Rev. B **15**, 298 (1977); **9**, 4897 (1974).
[27]S. -C. Lui, Ph.D. thesis, University of Pennsylvania, 1988.
[28]J. W. Davenport, Phys. Rev. B **29**, 2896 (1984).
[29]R. E. Watson, J. W. Davenport, and M. Weinert, Phys. Rev. B **34**, 8421 (1986).
[30]J. W. Davenport, R. E. Watson, and M. Weinert, Phys. Rev. B **37**, 9985 (1988).
[31]G. W. Fernando, J. W. Davenport, M. Weinert, and R. E. Watson, Phys. Rev. B **40**, 2757 (1989).
[32]M. Weinert, J. Math. Phys. **22**, 2433 (1981).
[33]A. R. Williams, J. Kubler, and C. D. Gelatt, Jr., Phys. Rev. B **19**, 6094 (1979).
[34]F. Cyrot, Adv. Phys. **16**, 393 (1967).
[35]B. P. Tonner, Nucl. Instrum. Methods **172**, 133 (1980).
[36]C. L. Allyn, T. Gustafsson, and E. W. Plummer, Rev. Sci. Instrum. **49**, 1197 (1978).
[37]D. M. Zehner and G. R. Gruzalski, in *Physical and Chemical Properties of Thin Metal Overlayers and Alloy Surfaces,* edited by D. M. Zehner and G. W. Goodman, Mater. Res. Soc. Symp. Proc. No. 83 (MRS, Pittsburgh, 1987), p. 199.
[38]M. H. Kang, S.-C. Lui, E. J. Mele, E. W. Plummer, and D. M. Zehner, Phys. Rev. B **41**, 4920 (1990).
[39]M. H. Kang, Ph.D. thesis, University of Pennsylvania, 1988.
[40]S.-C. Lui, M. H. Kang, E. J. Mele, E. W. Plummer, and D. M. Zehner, Phys. Rev. B **39**, 13 149 (1989).
[41]S. Hüfner, G. K. Wertheim, N. V. Smith, and M. M. Tram, Solid State Commun. **11**, 323 (1972).
[42]J. W. D. Connolly, Phys. Rev. **159**, 415 (1967).
[43]R. E. Watson and L. H. Bennett, in *Theory of Alloy Phase Formation* (AIME, Warrendale, PA, 1980), p. 425.
[44]A. Liebsch, Phys. Rev. Lett. **43**, 1431 (1979).
[45]C. Cuillot, Y. Ballu, J. Paigné, J. Lecante, K. P. Jain, P. Thiry, R. Pinchaux, Y. Pétroff, and L. M. Falicov, Phys. Rev. Lett. **39**, 1632 (1977).
[46]We did not observe any satellite structure in our valence-band measurement using photoemission.
[47]See Fig. 13.
[48]T.-C. Chiang, J. A. Knapp, M. Aono, and D. E. Eastman, Phys. Rev. B **21**, 3513 (1980).
[49]R. A. Bartynski, R. H. Gaylord, T. Gustafsson, and E. W. Plummer, Phys. Rev. B **33**, 3644 (1986).
[50]F. J. Himpsel, D. E. Eastman, and E. E. Koch, Phys. Rev. B **24**, 1687 (1981).
[51]J. A. Knapp, F. J. Himpsel, and D. E. Eastman, Phys. Rev. B **19**, 4952 (1979).
[52]L. Hedin, Phys. Rev. **139**, A796 (1965).
[53]M. Weinert, J. W. Davenport, and R. E. Watson, Phys. Rev. B **34**, 2917 (1986).
[54]J. W. Davenport (unpublished).
[55]A. Pasturel, P. Hicter, and F. Cyrot-Lackmann, J. Less-Common Met. **86**, 181 (1982).
[56]C. D. Gelatt, Jr., A. R. Williams, and V. L. Moruzzi, Phys. Rev. B **27**, 2005 (1983); D. N. Manh, D. Mayou, A. Pasturel, and F. Cyrot-Lackman, J. Phys. F **15**, 1911 (1985).
[57]D. Hackbracht and J. Kübler, J. Phys. F **10**, 427 (1980).
[58]M. Morihaga, N. Yukawa, and H. Adachi, J. Less-Common Met. **108**, 53 (1985).
[59]R. E. Watson, J. Hudis, and M. L. Perlman, Phys. Rev. B **4**, 4139 (1971).
[60]J. Hermanson, Solid State Commun. **22**, 9 (1977); W. Eberhardt and F. J. Himpsel, Phys. Rev. B **21**, 5572 (1980).
[61]See, for example, *Photoemission and the Electronic Properties of Surface,* edited by B. Feuerbacher, B. Fitton, and R. R. Willis (Wiley, New York, 1978).
[62]P. Thiry, O. Chandresis, J. Lecante, C. Guillot, R. Pinchaux, and Y. Petroff, Phys. Rev. Lett. **43**, 82 (1979).